

Project Description:

The main objective of this proposed research is to *provide state DOTs a practical and cost-effective long-term fatigue crack monitoring methodology using a **wireless elastomeric skin sensor network***. This research is intended to demonstrate the value-added of fatigue crack monitoring of steel bridges using wireless skin sensors over the traditional bridge inspection.

Progress this Quarter (includes meetings, work plan status, contract status, significant progress, etc.):*ISU Progress:*

Under this task, fatigue crack sensors are to be produced with an approximate thickness of 100-200 μm to enhance the mechanical robustness under harsh environment. Acceptable range of capacitance is 800-1000 pF. The anticipated number of sensors is 150 to 200 for the duration of the project.

During this quarter, 30 sensors of dimensions 1" x 1" have been fabricated. Technical support (Task 3) is being provided to KU on a continuous basis, as well as discussion and feedback (Task 4).

KU Progress:

KU continued to test the bridge girder subassembly model to evaluate the SEC network for monitoring distortion-induced fatigue cracks. Two strategies were evaluated, including using the SECs as direct crack sensors and using the SEC networks to capture the change of strain field due to crack propagation. In addition, KDOT has located a steel highway bridge as the testbed for field deployment.

UA Progress:

Arizona team has been focused on improving the shunt calibration of the sensor board. All sensor boards need to be calibrated to get correct measurements. For resistance-type strain sensors, traditional single shunt calibration method is sufficient for precise calibration because of low sensitivity to the parasitic resistance of lead wires. However, capacitive-type strain sensor (i.e. SEC) calibration is challenging because of high-sensitivity requirement, i.e., even with small parasitic resistance or capacitance in the lead wires, the lead wire effects can cause substantial error during the shunt calibration process.

To address this issue, a dual capacitor-based shunt calibration method has been developed and validated in combination with the SEC. For this shunt calibration, high-precision calibration-purpose ceramic capacitors have been used. Typical ceramic capacitors have 5~20% tolerance errors, but calibration capacitors have 1~2% tolerance errors. 5pF and 1pF calibration (high-precision) capacitors were used (i.e. 4pF difference), voltage changes corresponding to the capacitance variation (i.e. calibration coefficient) were calculated. Validation tests were conducted with stepwise sine excitation. The capacitance variation converted from the sensor board voltage measurement showed good agreement with the actual SEC capacitance variation.

Anticipated work next quarter:

ISU: Sensor production will continue in the next quarter. Technical support is being provided to KU on a continuous basis, as well as discussion and feedback.

KU: KU team will continue to finish testing the bridge subassembly model. Another bridge subassembly model will be tested with an updated sensor network configuration. Preliminary field test will also be conducted with the I-70 bridge.

UA: In the next quarter, Arizona team will continue to provide assistance to the KU team in terms of evaluating the sensor board at KU test setup.

Significant Results:

Part 1: Crack detection using the SEC sensor

The KU team continued to focus on testing the bridge girder-to-cross-frame connection (connection model) in this quarter. The progress is summarized as follows:

1. Test setup

Figure 1a and 1b shows the test setup which was presented in the last quarterly report. Figure 1c shows the arrangement of the dense SEC arrays at the connection model. Two sizes of SECs were used including large SECs with dimensions of 3 in. by 3 in., and small SECs of 1.5 in. by 1.5 in. A total of 24 SECs were deployed in the interior side of the connection (Figure 1c). On the exterior side of the connection, 4 new large SECs were attached at the top and bottom of the connection, respectively (Figure 1e). These 4 new SECs would be capable of monitoring strain field migration caused by crack growth. Figure 4d and 4f show the layout and the sensor numbers of the SEC arrays.

Cyclic fatigue load was applied through the actuator as shown in Figure 1a and 1b. The load cycles were 0.5 Hz harmonic signals with a range from -1.1 k to 1.1 k. To prevent out-of-plane movement of the cross frame when applying the load cycles, additional lateral constraints were added so that only vertical movement would occur at the cross frame, as illustrated in Figure 1a.

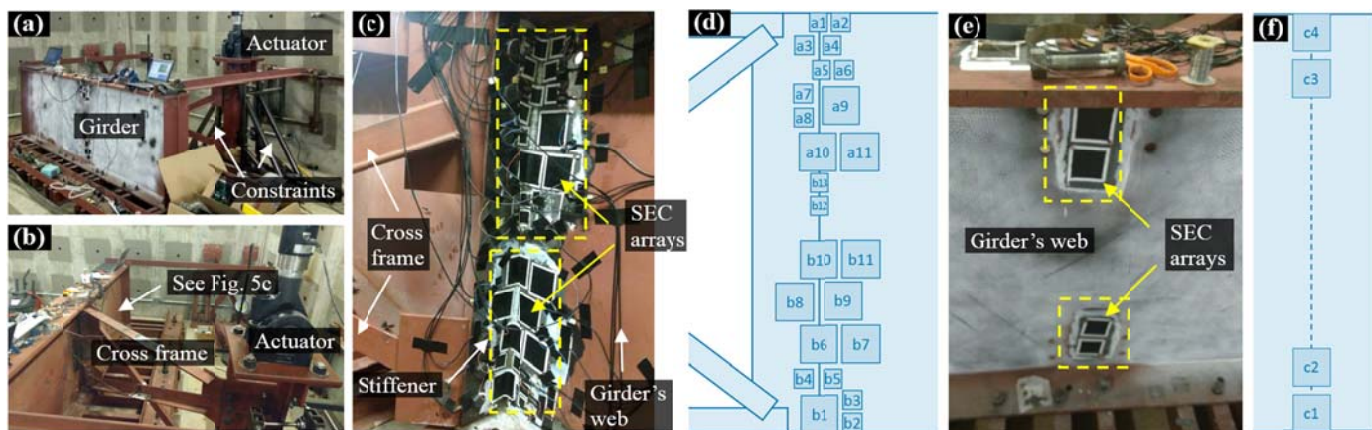


Figure 1. (a) Exterior view of the test model; (b) interior view of the test model; (c) SEC arrays and (d) sensor layout at the interior side of the connection; and (e) SEC arrays and (f) sensor layout at the exterior side of the connection.

Prior to the installation of the SEC arrays, the test model had been loaded with 2.7 million cycles with a load range of 0 to 2.5 k. Two out-of-plane fatigue cracks have been generated between the stiffener and web as shown in Figure 2a, 1b, and 1c. The top fatigue crack was about 0.75 in. (Figure 2b), while the bottom fatigue crack was about 1.5 in. (Figure 2c). The tips of fatigue cracks are denoted as yellow crosses in figures.

In field applications, the load applied to steel bridges caused by traffic may not be always known. One solution is to deploy strain gauges along the load path to indirectly infer the magnitude of loads. Because distortion-induced fatigue cracks are mainly induced by the differential vertical movements between two adjacent girders, the strains of the cross frame members are proportional to the external load. For this reason, a foil strain gauge was deployed on a diagonal member of the cross frame to indirectly capture the applied load as shown in Figure 2d and 2e.

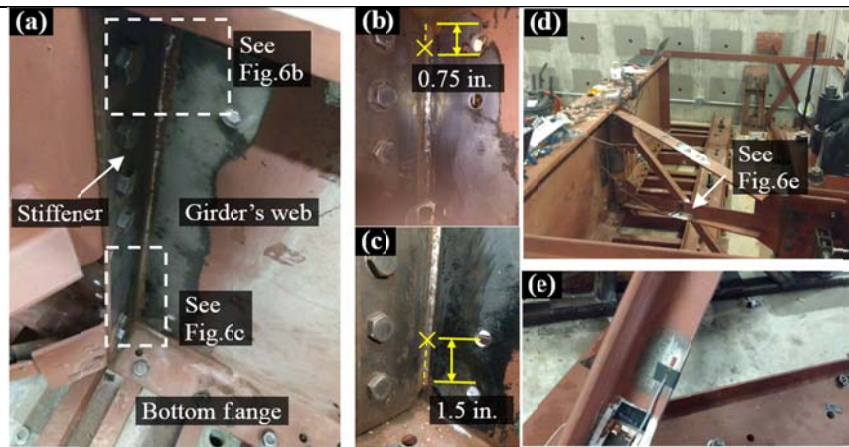


Figure 2. (a) Test model prior to sensor deployment; (b) an existing fatigue crack at the top of the connection; (c) an existing fatigue crack at the bottom of the connection; (d) and (e) a strain gauge was deployed on a diagonal member of the cross frame.

2. Test procedure

During the test, 71000 new cycles were applied to the test model and 8 datasets were collected when the new load cycle reached 0, 15000, 21500, 30000, 43100, 53800, 64900, and 71000, respectively. After 71000 cycles, SEC a1 and b1 (denoted in Figure 1d) were removed in order to closely inspect the propagated crack. As shown in Figure 3a, the length of the fatigue crack was 0.75 in. at the beginning of the test prior to the installation of the SEC arrays. When the test was done, the crack propagated to its new length of 1.65 in., indicating the fatigue crack propagated within the 8 data collection intervals. Similar phenomenon can be found in SEC b1 as shown in Figure 4. The crack grew from 1.5 in. to 3.5 in. during the test. Furthermore, both SEC a1 and b1 experienced damage as shown in the red circles in Figure 3 and Figure 4.



Figure 3. (a) The fatigue crack grew from 0.75 in. to 1.65 in. during the test; (b) front side of the SEC a1; (c) front side of the SEC a1 under stretching; (d) back side of the SEC a1; and (e) back side of the SEC a1 under stretching.

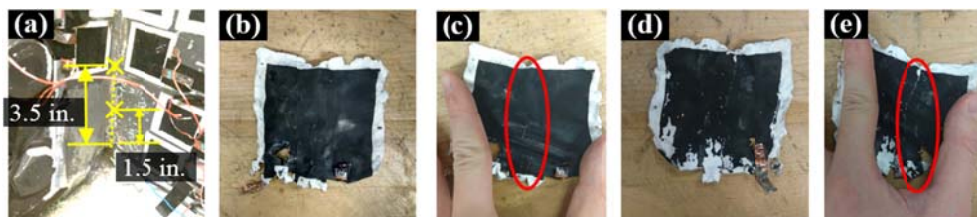


Figure 4. (a) The fatigue crack grew from 1.5 in. to 3.5 in. during the test; (b) front side of the SEC a1; (c) front side of the SEC a1 under stretching; (d) back side of the SEC a1; and (e) back side of the SEC a1 under stretching.

3. Method for constructing CGI map

Previously, a crack monitoring algorithm was established by the KU team which can extract fatigue damage feature, termed as crack growth index (CGI), from the measurements. In this quarter, we further extend this algorithm in a context of spatially distributed CGI maps.

Figure 5 shows an example of CGI map construction using the top region of the connection. Totally 11 SECs were deployed. The CGIs of these SECs can be first extracted by the previously established algorithm. Then, Linear interpolation was applied to these CGIs over the spatial dimensions x and y (denoted in Figure 5a) to create a 3D CGI surface as shown in Figure 5b. Essentially, the 3D CGI surface is a matrix containing the interpolated CGIs within the red-dashed zone in Figure 5a. Next, the 3D CGI surface is presented in terms of a 2D image, termed as CGI map in Figure 5c. The intensity of each pixel (x, y) in the CGI map is an interpolated CGI. The CGI map offers a clear presentation of the spatial distribution of CGI and serves as the basis of fatigue damage sensing using dense SEC arrays.

Finally, by periodically collecting short-time measurements from the monitored structure under the fatigue load cycles. A series of CGI maps can be constructed through the above procedure. If the fatigue crack does not propagate during the data collection intervals, the corresponding CGI maps would exhibit similar spatial intensities. On the other hand, if the fatigue crack grows in such intervals, it would provoke changes in the intensity distribution of the CGI map.

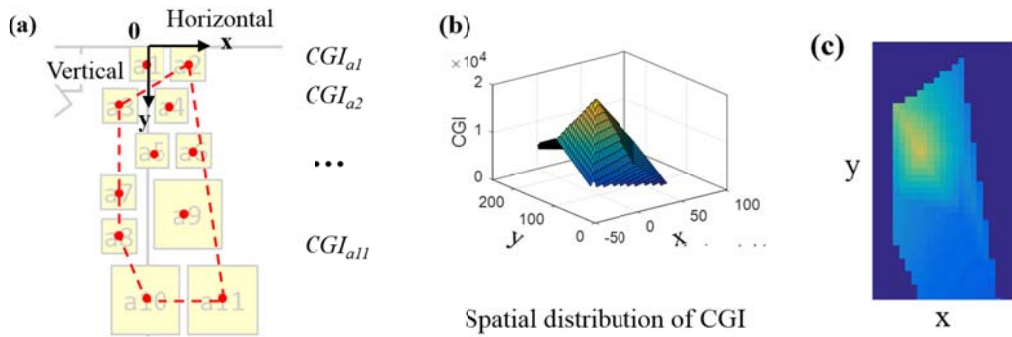


Figure 5. Construction of the CGI map.

4. Discussion on signal quality of SECs

Before the SEC measurements are processed for extracting CGIs, the signal quality of SEC arrays was evaluated. Figure 6 shows two typical measurements of SEC a1 before and after the sensor damage. As discussed previously, damage was found on the back side of SEC a1 after the test (Figure 3). As a result, the measurement from SEC a1 shows different behaviors as shown in Figure 6b. Figure 7 shows a typical measurement of SEC b1 after sensor damage. These results indicate that the existing fatigue cracks caused by the out-of-plane distortion could provoke shear-type deformation in the sensing material, leading to damage in SEC a1 and b1. For this reason, measurements of SEC a1 and b1 are not included in the CGI map construction.

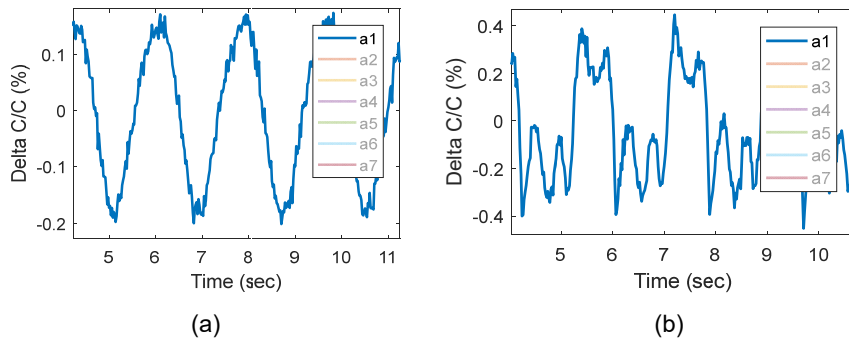


Figure 6. Typical measurements of SEC a1 (a) before and (b) after sensor damage

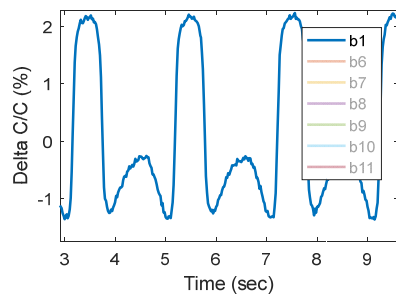


Figure 7. Typical measurement of SEC b1 after sensor damage

5. CGI from individual SECs

Utilizing our previously established algorithm, the CGI responses of SEC arrays on the top and bottom regions of the connection are shown in Figure 9 and Figure 10, respectively. As shown in Figure 9c, the top fatigue crack experienced propagation from 0.75 in. to 1.65 in. during the test. As a result, the SEC arrays demonstrate three different types of responses categorized as follows: 1) SEC a6, a7, a8, a9, and a11 show increasing trends in Figure 9a, indicating an increasing strain field caused by the downward movement of the crack tip; (2) response of SEC a2 continuously drops,

caused by the decreasing strain field along the crack path when the crack tip moved further; (3) SEC a3 and a4 demonstrate increasing trends before 30000 load cycles, after which decreasing trends can be found. This may indicate an increasing strain field around the crack tip provoked highest CGIs of SEC a3 and a4 around 30000 cycles and strain relief along the crack path induced lower CGIs after 30000 cycles.

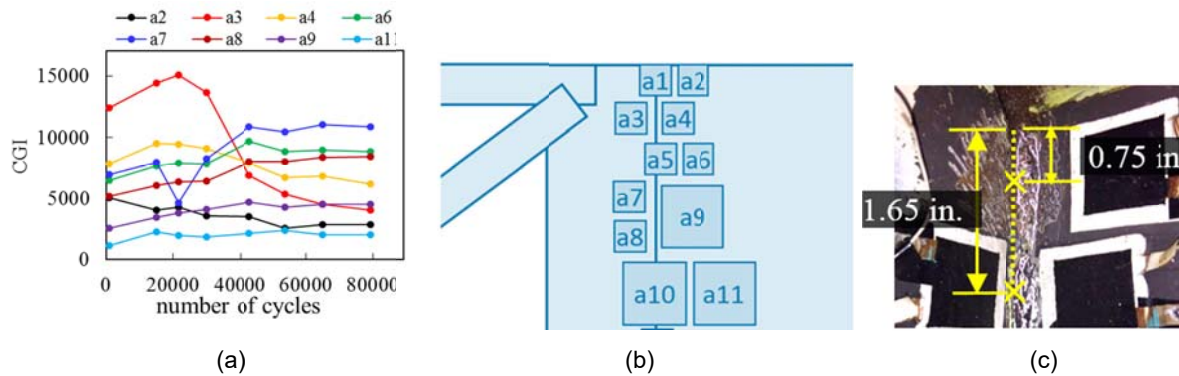


Figure 9. CGI responses from top region of the connection.

As shown in Figure 10c, the bottom fatigue crack propagation from 1.5 in. to 3.5 in. during the test. As a result, SEC arrays demonstrate two different types of responses categorized as follows: 1) SEC b4 and b5 demonstrate increasing trends of CGIs. This is caused by the increasing strain field provoked by the upward movement of crack tip; 2) other SECs in the bottom region of the connection have stable CGIs as they are deployed away from the crack growth path hence are less sensitive to the crack growth.

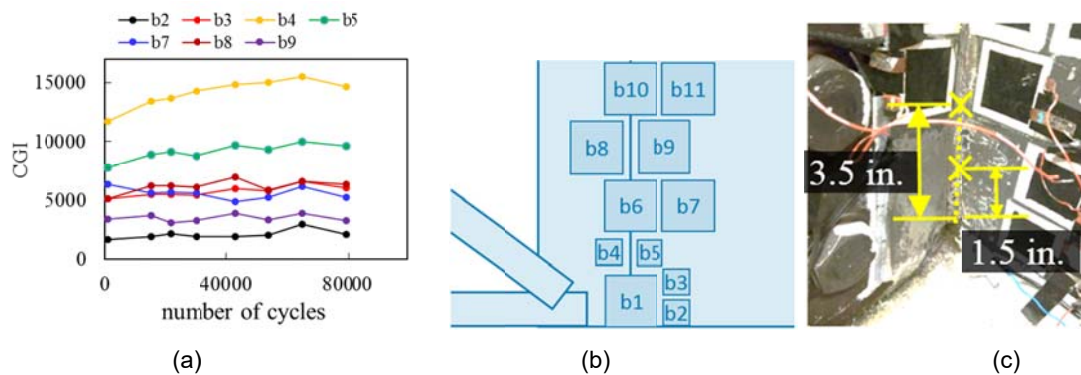


Figure 10. CGI responses from bottom region of the connection.

Finally, CGIs of SEC a5 and b6 are shown in Figure 11. Both CGIs demonstrate a much higher response than other SECs in the sensor arrays. This may be caused by the folded configuration of the sensors as the sensors would produce higher capacitance response due to the relative rotation between the stiffener and the girder.

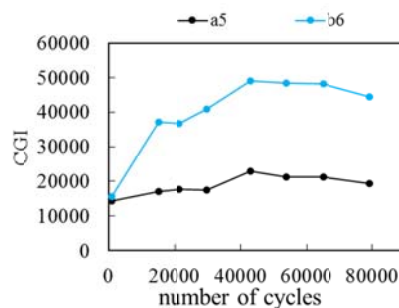


Figure 11. CGI responses of SEC a5 and b6.

7. CGI maps

7.1 CGI maps excluding SEC a5 and b6

Using the proposed method, CGI maps at different load cycles are shown in Figure 13 and 15. The magnitude of the CGI map is represented in term of $\log(\text{CGI})$. The regions of the CGI map are illustrated in Figure 12. The two folded SECs a5

and b6 are not included in the CGI maps.

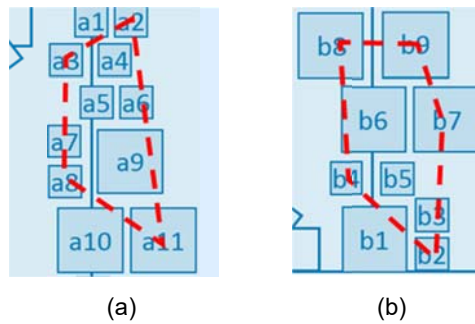


Figure 12. Regions of CGI maps at (a) top and (b) bottom of the connection.

As shown in Figure 10, the intensity of CGI at the top left corner changes between 30000 cycles and 43100 cycles, indicating the migration of the strain field. This further indicates the fatigue crack on the top of the connection propagates within these two data collection intervals.

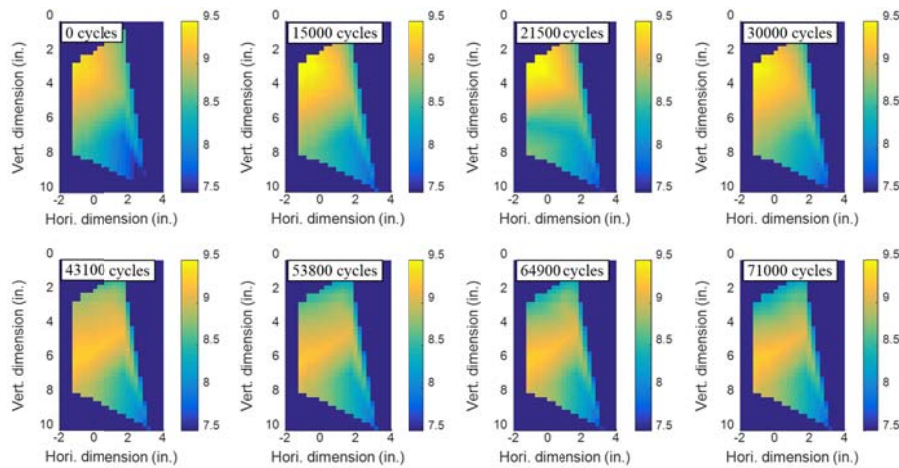


Figure 13. CGI maps from the top region of the connection.

Figure 13 compares the CGI maps at the beginning and end of the test, where only a particular range of CGI (from 8.6 to 9.5) is demonstrated. A clear shift of CGI intensities can be found in Figure 13, indicating the crack propagated during the test.

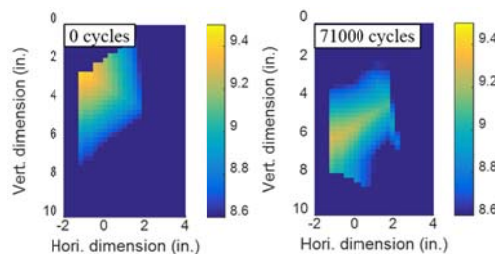


Figure 14. CGI maps of a particular range of CGI at the top region of the connection.

Figure 14 and Figure 15 illustrate the similar results for the bottom region of the connection. Even though the CGI changes are not as clear as in Figure 13, a particular region of the CGI map, as shown in Figure 15, moves upward during the test. This further indicates the CGI map can monitor the crack growth at the bottom region of the connection.

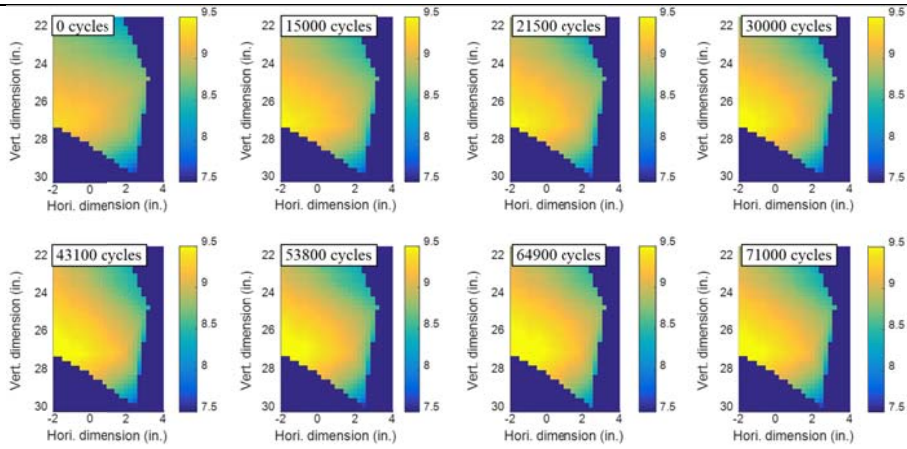


Figure 15. CGI maps from the bottom region of the connection.

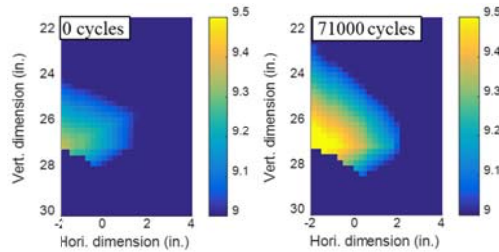


Figure 16. CGI maps of a particular range of CGI at the bottom region of the connection.

7.2 CGI maps including SEC a5 and b6

Figure 17 and 18 shows CGI maps including SEC a5 and b6, where similar trend of intensity change can be found in the top and bottom regions of the connection, respectively. Because of the high CGI magnitudes of SEC a5 and b6, these two sensor locations in the CGI maps show brighter color.

Figure 17 shows the CGI maps including SEC a5 and b6.

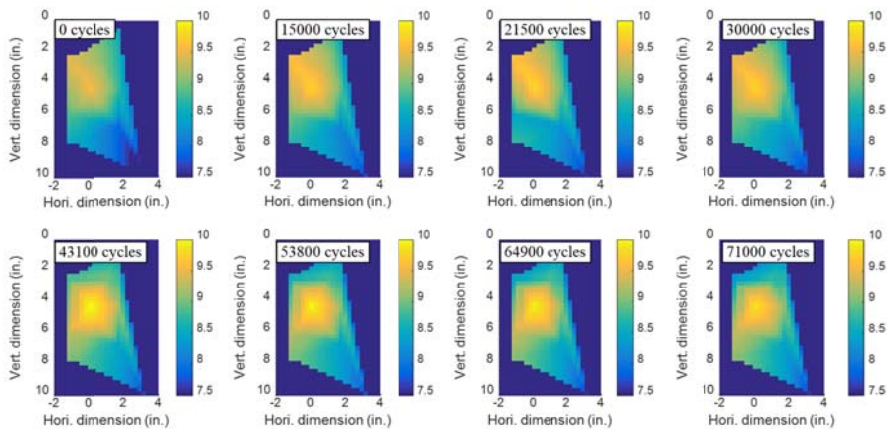


Figure 17. CGI maps from the top region of the connection.

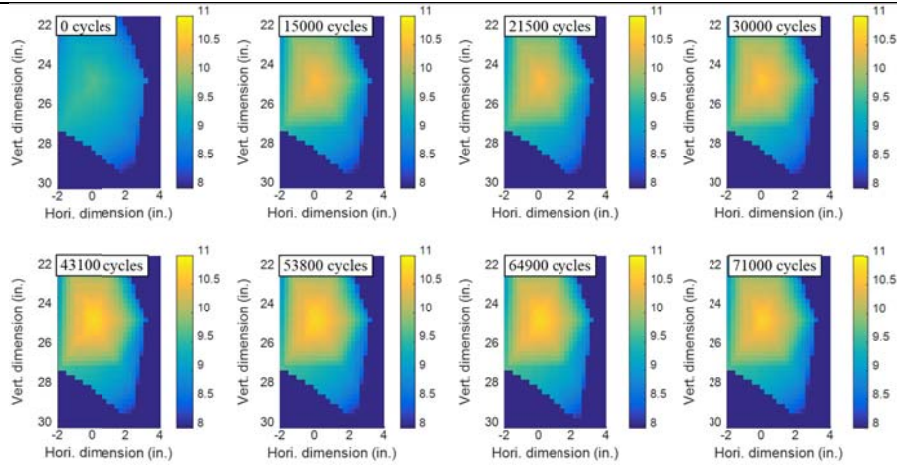


Figure 18. CGI maps from the bottom region of the connection.

Part 2: Wireless data acquisition

The main results from the University of Arizona team are presented as follows.

Modified shunt calibration was developed and validated. In practical applications, every sensor board has different bridge balances and amplifications, thus calibration is necessary before actual application to know the exact changes of sensor capacitances. To convert voltage measurement from sensor board to actual SEC capacitance change, two capacitors were used other than a single capacitor, because SEC variation response is sensitive to parasitic resistance and capacitance of lead wires. A modified shunt calibration using two capacitors allows measuring pure SEC capacitance variation by a two-step shunt calibration procedure.

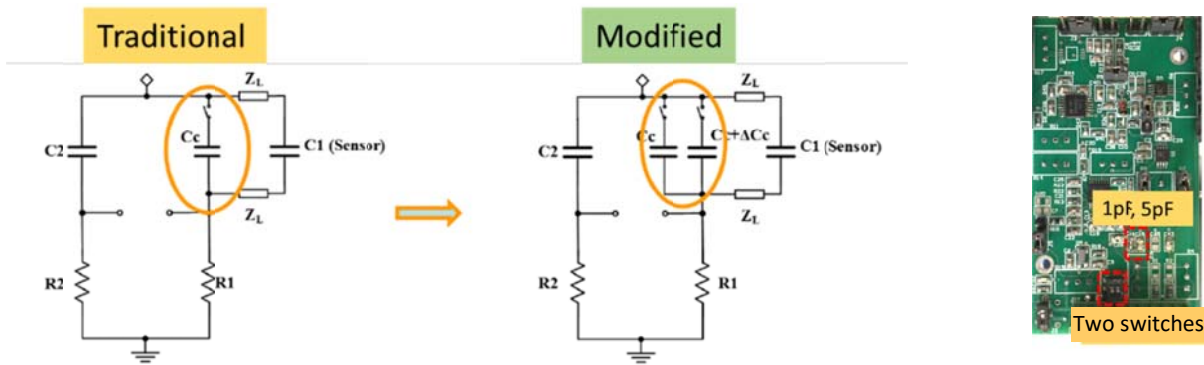


Figure 19. Modified shunt calibration structure and board

Figure 19 shows the schematic of the modified shunt calibration circuit on the sensor board composed of two reference capacitors and two switches. The capacitance values for calibration need to be selected appropriately. Signal in the sensor board can be easily saturated depending on the capacitance variation during calibration because of high amplification level to be used. To avoid saturation, calibration capacitance range should be considered based upon capacitor's specification and measurement range. Also, the calibration capacitors need to be high-precision ones. Usual commercial capacitors have 5% to 20% tolerance. However, considering capacitance variance range of SEC is around 0.1% (0.75pF for a 750pF-SEC), high-precision capacitors must be used to avoid calibration error. Figure 20 shows the example of the selected capacitors for calibration purpose.



Figure 20. High precision capacitor

The values of the calibration capacitors were selected as 1pF and 5pF, which are the optimized values for possible capacitance variations of the SEC for this project. To validate the dual-capacitor shunt calibration, two different bridge balancing and amplification cases were tested. Calibration coefficients were calculated based on calibration test measurement shown in Figure 3 below. Test procedure is described below

1. Start measurement (0 to 4 sec. in Fig. 21(a))
2. Turn on 5pF switch (adds 5pF to measurement 4 to 11 sec. in Fig. 21(a)) and turn off (11 to 16sec in Fig. 21(a))
3. Turn on 1pF switch (adds 1pF to measurement 17 to 24 sec. in Fig. 21(a)) and turn off
4. Repeat the above procedure to get an averaged coefficient.

By adopting the two-step shunt calibration, pure capacitance variation without parasitic capacitance/resistance effects were successfully achieved.

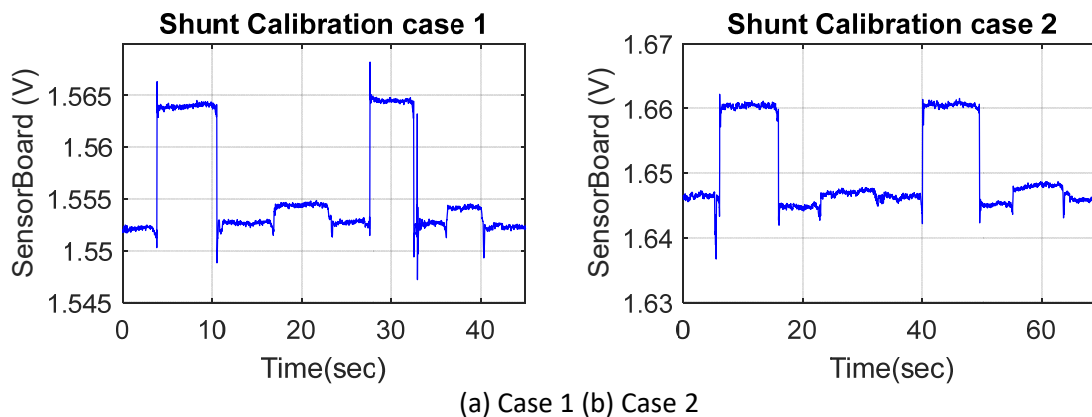
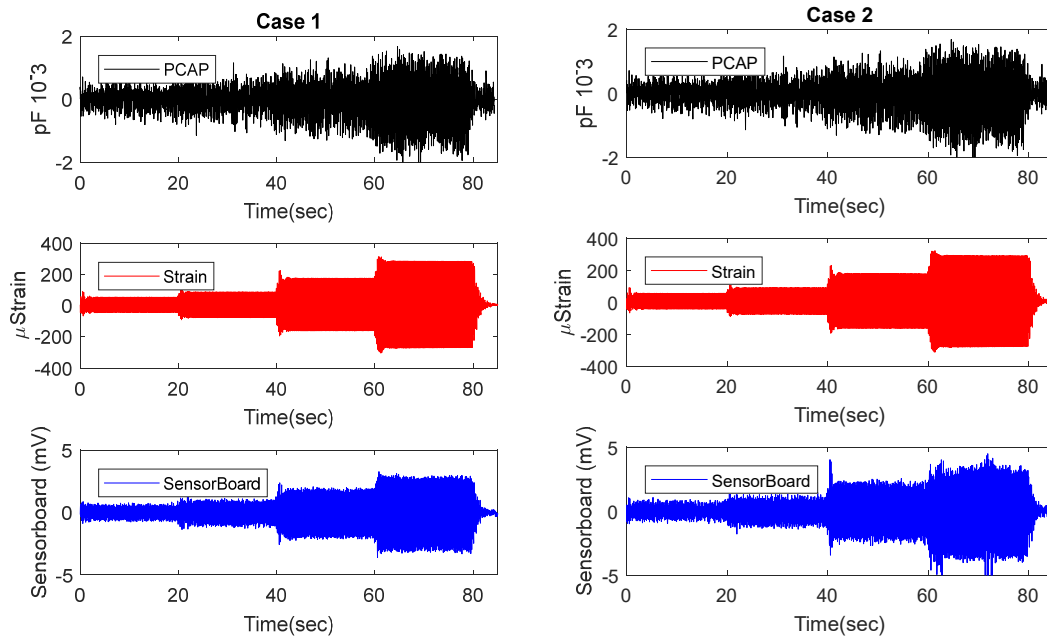


Figure 21. Two step calibration result

Using this result, users can estimate voltage variation from the 4pF (5pF – 1pF) change in SEC. From two shunt calibration tests, voltage to capacitance conversion coefficient of 2.35 mv/pF and 3.25 mv/pF were achieved for the two test cases, respectively. To validate the linearity and accuracy, shake table tests were conducted using the 4-step incremental sine wave excitation. The same 4-step sine wave excitation was used for both case 1 and case 2.



(a) Case 1 (b) Case 2
 Figure 22. Incremental sine wave excitation test results

Incremental sine wave excitation tests were conducted as shown in Figure 22. Top row signals are capacitance change measured by PCAP and red signals are (foil-type) strain gauge measurements, blue signals are measurements from the sensor board. Four step sine excitations were applied every 20sec for 80, 150, 300, 550 micro strain.

Figure 23 shows calculation example that compared capacitance variation versus voltage change measured in the tests.

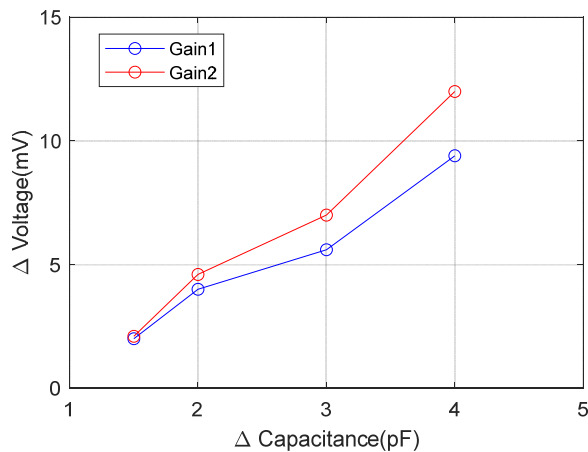


Figure 23. Capacitance variance versus voltage measurement

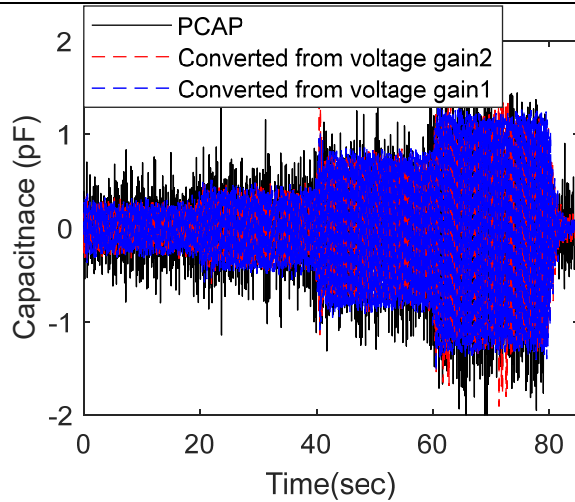


Figure 24. Reconstructed capacitance from validation tests

Using the calibration coefficients, the reconstructed capacitance data from voltage in two validation tests shows good agreement in Figure 24. The solid red line is from test case 2 and the dashed blue line is from test case 1. The two converted measurements match well and show cleaner data than the commercial capacitance measurement kit (PCAP) shown as black solid line.

Circumstance affecting project or budget. (Please describe any challenges encountered or anticipated that might the completion of the project within the time, scope and fiscal constraints set forth in the agreement, along with recommended solutions to those problems).

None.